NANO LETTERS

2009
Vol. 9, No. 12
4505-4509

Manipulating Nanoscale Light Fields with the Asymmetric Bowtie Nano-Colorsorter

Z. Zhang,[†,‡] A. Weber-Bargioni,[†] S. W. Wu,[†] S. Dhuey,[†] S. Cabrini,[†] and P. J. Schuck*[,†]

Molecular Foundry, Lawrence Berkeley National Lab, Berkeley, California 94720, and Department of Chemistry, UC Berkeley, Berkeley, California 94720

Received August 31, 2009; Revised Manuscript Received October 13, 2009

ABSTRACT

We present a class of devices called Asymmetric Bowtie nano-Colorsorters. These devices are specifically engineered to not only capture and confine optical fields, but also to spectrally filter and steer them while maintaining nanoscale field distributions. We show that spectral properties and localized spatial mode distributions can be readily tuned by controlled asymmetry. Nano-Colorsorters can control light's spatial and spectral distributions at the nanoscale and thus significantly impact applications ranging from broadband light harvesting to ultrafast wavelength-selective photodetection.

A central goal of plasmonics is complete control over optical signals at deeply subwavelength scales. The recent invention of optical nanoantennas has led to a number of device designs that provide confinement of optical fields at nanometer length scales.[1−13] For photonic applications, however, the effectiveness of these structures would be significantly improved by the added ability to spatially sort the optical signals based on a physically accessible parameter such as energy/color.[14−18] Here, we present our experimental and theoretical study of a class of devices, termed Asymmetric Bowtie nano-Colorsorters (ABnC), which demonstrate both the ability to efficiently capture and strongly confine broadband optical fields, as well as to spectrally filter and steer them while maintaining nanoscale field distributions. The latter property is important because it allows for manipulation while preserving the physical match, created by the optical antenna, between the localized field distribution and important physical factors such as semiconductor carrier diffusion lengths and zeptoliter volumes occupied by individual nano- and quantum- objects. Because of these capabilities, ABnCs are expected to have a profound impact on a wide range of optoelectronic and plasmonic applications including ultrafast color-sensitive photodetection, solar power light harvesting, super-resolution imaging, and multiplexed chemical sensing.

Our proof-of-principle ABnC devices are based on asymmetric variations of double-bowtie nanoantennas oriented in a "cross" geometry. As an essential experimental complement to our theoretical modeling, an initial step of our investigation was to demonstrate the feasibility of fabrication of these devices. The nanoantennas are fabricated using electron-beam lithography (Vistec VB300, 100 keV beam energy) and lift-off on indium−tin−oxide- (ITO) coated fused silica substrates (ITO thickness = 50 nm) and consist of approximately 17 nm thick Au on top of a 3 nm Ti adhesion layer. Each constituent Au triangle in the cross nanoantenna is designed to be equilateral in shape with a perpendicular bisector length of 75 nm. Experimentally, the nanoantenna resonances are measured by collecting darkfield scattering spectra from individual structures in a transmission confocal modality: white light is focused on the back of the transparent sample with a high numerical aperture (N.A.) oil condenser (N.A. = 1.43−1.2) and scattered light is collected with a 100×, 0.95 N.A. air objective, focused through a 150 μm diameter pinhole, then directed into 0.3 m spectrometer (PI-Acton) and dispersed onto a liquid-nitrogen-cooled charge-coupled device (CCD) camera.

Calculations of the fields surrounding our devices were done using finite element method (FEM) software from COMSOL. Our analyzed volume consisted of a 500 nm (x axis) × 500 nm (y axis) × 250 nm (z axis) top layer of air (index of refraction, n, = 1), a 500 nm × 500 nm × 50 nm middle layer of ITO (n_{ITO} = 1.91), and a 500 nm × 500 nm × 250 nm bottom layer of glass (n_{glass} = 1.5). Perfectly matched layers (PML) surrounded the volume (100 nm thick for the sides, 250 nm thick at the bottom). Twenty nanometer thick Au nanoantennas and ABnC devices were placed

* To whom correspondence should be addressed. E-mail: pjschuck@lbl.gov.
† Lawrence Berkeley National Lab.
‡ UC Berkeley.

10.1021/nl902850f CCC: $40.75
Published on Web 11/09/2009

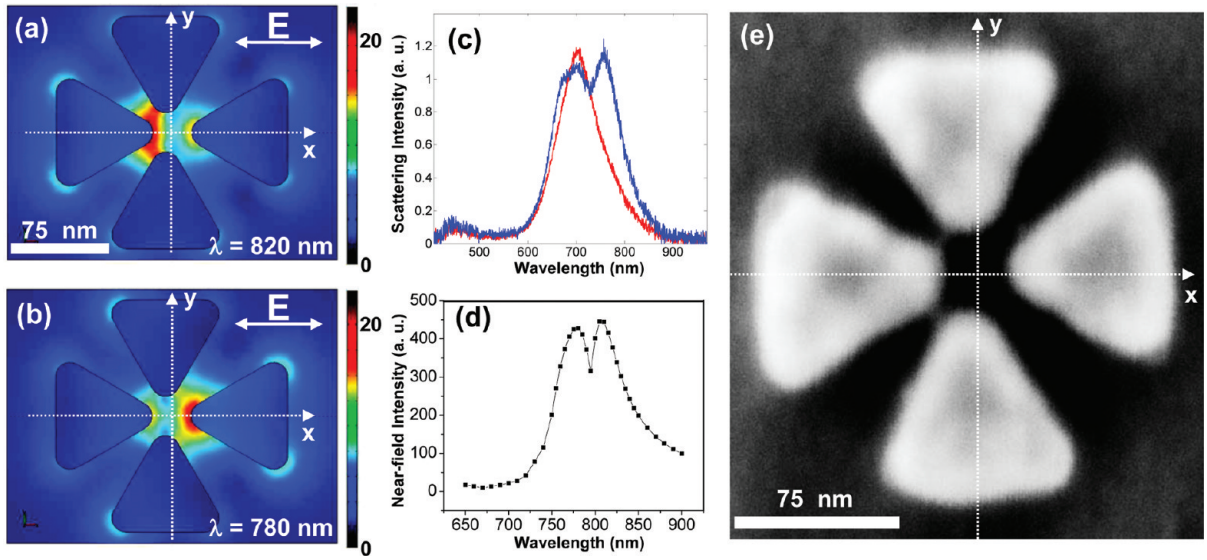

Figure 1. Calculated images of the e-field distributions surrounding an ABnC (*y*-oriented "vertical" bowtie component shifted 5 nm left-of-center) when excited at (a) 820 nm and (b) 780 nm. Note that the two modes are spectrally and spatially distinct while maintaining nanoscale mode volumes. This ABnC retains a reflection symmetry axis oriented along the *x*-axis. (c) Experimental dark-field scattering spectra from (blue) the ABnC shown in (e) and (red) a representative symmetric cross nanoantenna for comparison. (d) Calculated near-field intensity spectrum from the ABnC designed with the 5 nm vertical bowtie shift shown in (a) and (b). (e) Scanning electron microscope image of an ABnC with it's vertical bowtie component shifted ~5 nm left-of-center.

directly on the ITO layer, and all triangles had 10 nm radii of curvature at the corners. These parameters are very close to the specifications of the fabricated devices.[19] The wavelength-dependent dielectric constant used for the Au was taken from Palik et al.[20] Plane wave continuous excitation was incident from the top (air side) with electric field component amplitudes of $e_x = 1$, $e_y = 0$, $e_z = 0$. All calculated field distribution images are plots of normalized electric field (e-field) amplitude in a plane that cuts through the center of the devices' thickness (i.e., a plane with z set to 10 nm above the Au/ITO interface). Calculated near-field intensity spectra are plots of the maximum normalized e-field amplitude within this plane at each wavelength. We note that for experimental applications (e.g., nanoscale photodetectors[21] and nanoantenna-based near-field scanning probes,[22,23]) the relevant fields are those located directly in and just outside the nanoantenna gap region,[24,25] which is why the near-field spectral and spatial distribution information is calculated and presented here.

To help lend insight into the ABnC, we start by briefly describing the main resonance properties of the symmetric "cross" nanoantenna structure (C_{4v} symmetry), an example of which is shown in the Supporting Information Figure S1 (more detailed discussion of symmetric "cross" nanoantennas can be found in ref 26). An experimental darkfield scattering spectrum from an individual symmetric cross nanoantenna is also shown in Figure 1 (red curve) with the incident white light linearly polarized in the *x*-direction. The main mode primarily resembles the dipolar mode of a single bowtie that is excited with e-field polarization oriented parallel to the bowtie axis.[19,27] A weak shoulder on the blue side of the peak is also present, which is due to the *x*-polarized light interacting with the *y*-oriented "vertical" bowtie component of the cross (see refs 19 and 27 and Supporting Information).

When *x*-polarized incident light is energetically resonant with the primary dipole nanoantenna mode (at the wavelength corresponding to the red curve peak in Figure 1c), the calculated e-field distribution (normalized e-field amplitude) surrounding the symmetric cross is symmetric as well (Figure S1). As expected, the most intense fields are located near the tips of the two triangles comprising the horizontal bowtie.[26] This is consistent with the near-field distribution associated with simple bowtie nanoantennas with similar gap sizes,[28] though the local intensity near the center of the structure falls off more quickly in the *y*-direction due to added confinement by and interaction with the vertical bowtie.

Next, we use an asymmetric bowtie "cross" nanoantenna to demonstrate the basic principles of an ABnC (Figure 1). In this case, the asymmetry has been created by moving the *y*-oriented "vertical" bowtie component of the cross left-of-center by 5 nm, thereby reducing the cross symmetry from C_{4v} to C_s (i.e., the ABnC now has only one symmetry axis). The effect of this symmetry-breaking can be seen in the field distributions and the scattering spectrum shown in Figure 1. By shifting the "vertical" bowtie to the left only a few nanometers, the degeneracy of the nanoantenna's primary (polarization-aligned dipole) plasmon resonance mode breaks into two, which is observed as a doublet in the scattering spectrum (Figure 1c, blue curve) and calculated near-field intensity spectrum (Figure 1d). The small differences in experimental versus theoretical peak wavelengths are due primarily to small discrepancies in (1) the ITO dielectric constant and (2) metal particle sizes between the real values and those used in our FEM modeling.

The normalized e-field distributions for each of these two resonant peaks are shown in Figure 1a,b. It is clear that each resonance not only possesses a spatially distinct field distribution, but also retains a nanoscale mode volume. Each

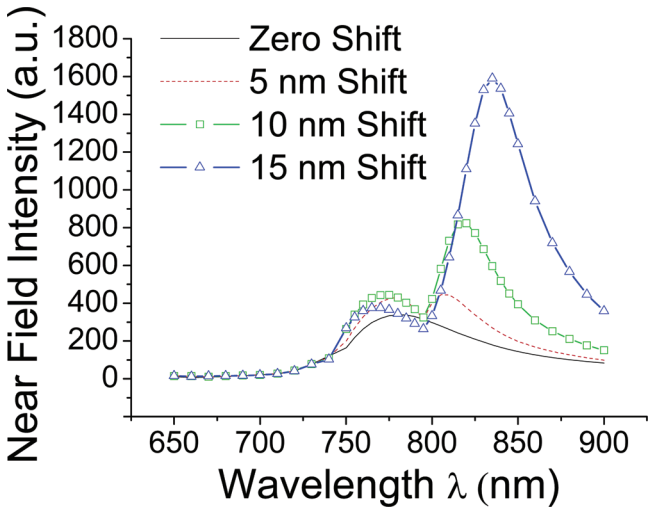

Figure 2. Calculated near-field intensity spectra for ABnCs in which the vertical bowtie component has been shifted horizontally by 0 nm (i.e., symmetric cross; black curve), 5 nm (red), 10 nm (green), and 15 nm (blue).

of these zeptoliter volumes can be individually addressed simply by adjusting the incident wavelength.

It is straightforward to tune the spectral shift between the two modes; it is simply controlled by changing how far the vertical bowtie is translated (in the left or right direction for horizontally polarized light) from center (i.e., by increasing the asymmetry and controlling the gap sizes between the constituent parts of the nanoantenna). The effects of shifting the vertical bowtie by 5, 10, and 15 nm, respectively, on the near-field intensity spectral response of the ABnC are illustrated in Figure 2. The peak wavelengths of both modes change as a function of vertical bowtie shift. When the vertical bowtie is moved left-of-center by 15 nm the high-energy mode blueshifts by a total 13.4 nm, while the low energy mode displays a marked redshift of 54 nm, demonstrating clear coupling between ABnC components.

Both modes result from the interactions between all constituents of the ABnC, though symmetry breaking affects the modes in different ways. These behaviors can be understood by examining the spatial field distribution associated with each mode (Figure 1a,b). As the vertical bowtie shifts away from the right-hand triangle, the coherent coupling between the right-hand triangle and the other ABnC components decreases, leading to the relatively weak spectral shift as a function of increasing asymmetry (i.e., weaker interactions result in less sensitivity to component arrangements). This also explains why the mode associated with the shorter-wavelength peak in the doublet bears similarity to the dipole resonance mode of an isolated triangle (Supporting Information). On the other hand, the longer-wavelength mode is more hybridized in nature.[29] In this case, the increase in coherent coupling energy, resulting from the decreasing (and small) gap sizes, between the three triangles on the left in Figure 1a dominates the mode properties. In the context of the plasmon hybridization model, the increased coupling energy manifests itself as an increased redshift in the lowest energy mode (dipolar-like in this case, which is why it is clearly observed in the scattering spectra). Note that the electric field enhancement for this mode also increases with decreasing gap size (increased asymmetry), as expected.

It is important to emphasize, however, that each mode originates from the complex coupling between all constituents comprising an ABnC. In fact, this is what makes the concept of the nanocolorsorter so powerful, resulting in the high degree of control over the spectral and spatial properties through symmetry engineering. The significance of the interplay between each ABnC part is verified by changing the arrangement of the components, while retaining the overall symmetry. The breaking of the dipolar mode degeneracy into two spectrally and spatially distinct modes is a behavior that occurs not only when the single reflection symmetry axis lies along the x-direction (and parallel to the incident E-field orientation), but also more generally when the reflection symmetry axis is rotated in the $x-y$ plane (i.e., whenever C_s symmetry is maintained). In Figure 3, we have created an ABnC with its symmetry axis rotated 45° by first shifting the y-oriented vertical bowtie of the cross left (by 5 nm in this case) and then up (by 5 nm). The experimental scattering spectrum (Figure 3c) and calculated near-field enhancement spectrum (Figure 3d) both still exhibit the signature doublet peaks (excitation is x-polarized). Clearly it is the overall arrangement/symmetry of the ABnC that determines the spectral mode structure, confirming the importance of all interacting components in defining the properties of the device. Field distributions associated with each of the two peaks remain localized and separated spatially from one another, though the exact spatial nature of the modes differs from that of the ABnC in Figure 1 due to the changed geometry.

The ABnC with its multiple metallic nanostructures separated by nanoscale gaps is also an example of a plasmonic molecule. A number of recent publications have discussed simple asymmetric plasmonic molecule geometries, showing that Fano resonances, often created by broken-symmetry-permitted optical interactions of bright and dark modes, result in intricate (and tunable) spectral behavior.[30−35] This is certainly also the case in the context of the ABnC, where fano-like resonances are observed in the spectral response. One particular advantage of the cross geometry is that it allows for strong interactions with all polarization states,[26] as well as for efficient cross-coupling of an x-polarized incident field into modes with significant y-oriented components (and vice versa).

We note that the device described above is a two-color ABnC. However, one can easily extend the sorting/multiplexing functionality to a greater number of wavelengths by designing the device to possess more asymmetric degrees of freedom. On the basis of the plasmon interactions that dictated the properties of the two-color ABnC discussed above, we have simulated the properties of a more asymmetric device designed to have three spatially and spectrally distinct modes (Figure 4). Here, we exchanged the bottom triangle of the cross for an ellipse (major axis = 50 nm, minor axis = 25 nm), moved it between the tips of the

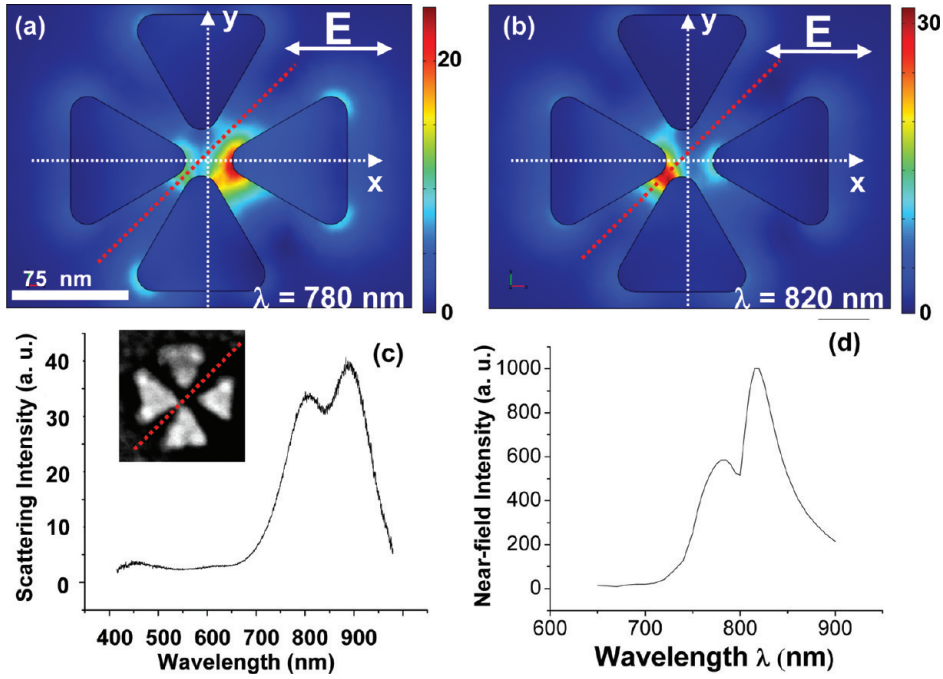

Figure 3. Calculated images of the e-field distributions surrounding an ABnC designed to have its reflection symmetry axis rotated 45° from the *x*-axis when excited at (a) 780 nm and (b) 820 nm. The dotted red lines in (a), (b) and inset of (c) mark the reflection symmetry axis. (c) Experimental dark-field scattering spectrum and (d) calculated near-field intensity spectrum from the ABnC with this symmetry. Inset of (c) is an SEM image of the ABnC device from which the scattering spectrum in (c) originated. Note that, as in Figures 1 and 2, retention of a single reflection symmetry axis in the cross ABnC design results in two spatially and spectrally distinct modes.

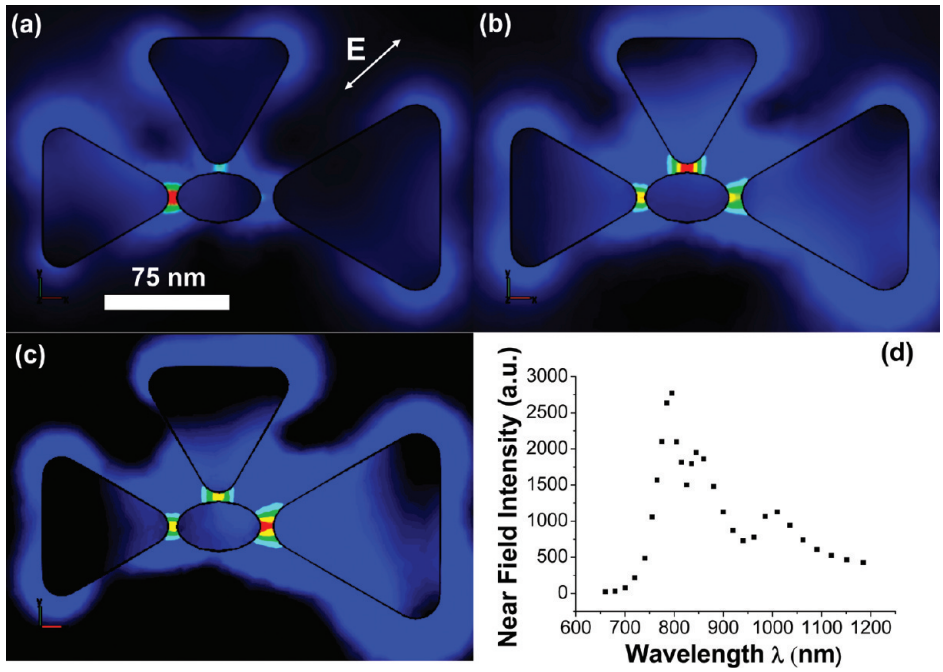

Figure 4. An example of an ABnC with an increased number of asymmetric degrees of freedom. Images of calculated field distributions showing spatially distinct field confinements due to mode hybridizations at (a) the left triangle-ellipse gap, (b) the top triangle-ellipse gap, and (c) the right triangle-ellipse gap. (d) The calculated near-field intensity spectrum from this device, which now exhibits three spectral modes (rather than two) due to the increased asymmetry.

remaining triangles, and enlarged the right-most triangle (perpendicular bisector = 100 nm). In addition, the incident radiation polarization is rotated 45° from the *x* axis in the calculations. This device design allowed us to engineer hybridized modes between (a) the long axis of the ellipse and a 75 nm triangle, (b) the short axis of the ellipse and a 75 nm triangle, and (c) the long axis of the ellipse and a 100 nm triangle. Because of the complexity of this device, combinations of these modes and higher-order modes are also present (see Supporting Information, supplementary movie). The calculated plasmon mode near-field spectra for the individual constituents of this device (75 nm triangle,

100 nm triangle, and ellipse) are given in the Supporting Information. The near-field enhancement spectrum calculated for this device is presented in Figure 4d. Three peaks are observed in the spectrum, clearly demonstrating the extension of the basic two-color ABnC to multiple wavelengths.

The fact that spatially distinct, nanoscale mode volumes can be individually addressed by tuning wavelength is of considerable importance to technological applications such as multicolor photon detection and sorting (e.g., red−green−blue (RGB) photodetectors). There are significant advantages to scaling photodetectors down to the nanoscale in all three dimensions, including efficiency and modulation speed.[21,36] When implemented in conjunction with an ABnC, these advantages are combined with near-unity collection efficiency afforded by the optical nanonantenna (and subwavelength device footprint), necessitating the design of high-density, ultrafast multicolor detector arrays.

In conclusion, we have shown that with the ABnC category of devices it is now possible to collect, concentrate, and manipulate optical fields all while maintaining deeply subwavelength field distributions. This is accomplished by engineering the internal symmetries of nanoantenna structures such that their constituent metallic elements create hybridized modes at selected positions and wavelengths. Because of the tunability and controllability of the localized optical fields, we expect these specifically designed plasmonic molecules to be useful for a wide range of multicolor photodetection and optical/plasmonic filtering/sorting applications.

Acknowledgment. We would like to thank B. Sanii, J. Neaton, A. McLeod, P. Ashby, S. Aloni, D. F. Ogletree, and M. Salmeron for insightful discussions, and A. Jamshidi and M. Staffaroni for COMSOL assistance. Work at the Molecular Foundry was supported by the Office of Science, Office of Basic Energy Sciences, of the U.S. Department of Energy under Contract No. DE-AC02-05CH11231. Z.Z. was also supported by the Defense Advanced Research Projects Agency (Nanoscale Architectures for Coherent Hyper-Optic Sources program).

Supporting Information Available: Related plasmonic nanostructure field distributions and spectral responses, as well as a movie of e-fields (from high- to low-energy excitation) surrounding 3-color ABnC, is given. This material is available free of charge via the Internet at http://pubs.acs.org.

References

(1) Schuck, P. J.; Fromm, D. P.; Sundaramurthy, A.; Kino, G. S.; Moerner, W. E. *Phys. Rev. Lett.* **2005**, *94*, 017402−4.
(2) Muhlschlegel, P.; Eisler, H. J.; Martin, O. J. F.; Hecht, B.; Pohl, D. W. *Science* **2005**, *308*, 1607–1609.
(3) Kuhn, S.; Hkanson, U.; Rogobete, L.; Sandoghdar, V. *Phys. Rev. Lett.* **2006**, *97*, 017402−4.
(4) Taminiau, T. H.; Moerland, R. J.; Segerink, F. B.; Kuipers, L.; van Hulst, N. F. *Nano Lett.* **2007**, *7*, 28–33.
(5) Novotny, L. *Phys. Rev. Lett.* **2007**, *98*, 266802.
(6) Cubukcu, E.; Kort, E. A.; Crozier, K. B.; Capasso, F. *Appl. Phys. Lett.* **2006**, *89*, 093120−3.
(7) Wang, H.; Wu, Y.; Lassiter, B.; Nehl, C. L.; Hafner, J. H.; Nordlander, P.; Halas, N. J. *Proc. Natl. Acad. Sci. U.S.A.* **2006**, *103*, 10856–10860.
(8) Behr, N.; Raschke, M. B. *J. Phys. Chem. C* **2008**, *112*, 3766–3773.
(9) Schnell, M.; Garcia-Etxarri, A.; Huber, A. J.; Crozier, K.; Aizpurua, J.; Hillenbrand, R. *Nat. Photonics* **2009**, *3*, 287–291.
(10) Kang, J. H.; Kim, D. S.; Park, Q. H. *Phys. Rev. Lett.* **2009**, *102*, 093906.
(11) Conway, J. A. Ph.D. Thesis, University of California, Los Angeles, 2006.
(12) Li, K. R.; Li, X. T.; Stockman, M. I.; Bergman, D. J. *Phys. Rev. B* **2005**, *71*, 115409.
(13) Ghenuche, P.; Cormack, I. G.; Badenes, G.; Loza-Alvarez, P.; Quidant, R. *Appl. Phys. Lett.* **2007**, *90*, 041109.
(14) Malyshev, A. V.; Malyshev, V. A.; Knoester, J. *Nano Lett.* **2008**, *8*, 2369–2372.
(15) Laux, E.; Genet, C.; Skauli, T.; Ebbesen, T. W. *Nat. Photonics* **2008**, *2*, 161–164.
(16) Kang, Z.; Wang, G. P. *Opt. Express* **2008**, *16*, 7680–7685.
(17) Choi, S. B.; Park, D. J.; Jeong, Y. K.; Yun, Y. C.; Jeong, M. S.; Byeon, C. C.; Kang, J. H.; Park, Q. H.; Kim, D. S. *Appl. Phys. Lett.* **2009**, *94*, 063115.
(18) Hao, F.; Sonnefraud, Y.; Van Dorpe, P.; Maier, S. A.; Halas, N. J.; Nordlander, P. *Nano Lett.* **2008**, *8*, 3983–3988.
(19) Sundaramurthy, A.; Crozier, K. B.; Kino, G. S.; Fromm, D. P.; Schuck, P. J.; Moerner, W. E. *Phys. Rev. B (Condens. Matter Mater. Phys.* **2005**, *72*, 165409–6.
(20) Palik, E. D. *Handbook of Optical Constants*; Academic Press: New York, 1985.
(21) Tang, L.; Kocabas, S. E.; Latif, S.; Okyay, A. K.; Ly-Gagnon, D. S.; Saraswat, K. C.; Miller, D. A. B. *Nat. Photonics* **2008**, *2*, 226–229.
(22) Farahani, J. N.; Pohl, D. W.; Eisler, H. J.; Hecht, B. *Phys. Rev. Lett.* **2005**, *95*, 017402.
(23) Weber-Bargioni, A.; Schwartzberg, A.; Schmidt, M.; Harteneck, B.; Ogletree, D. F.; Schuck, P. J.; Cabrini, S. submitted for publication, 2009.
(24) Chang, S. W.; Chuang, S. L. *Opt. Lett.* **2009**, *34*, 91–93.
(25) Hill, M. T.; Marell, M.; Leong, E. S. P.; Smalbrugge, B.; Zhu, Y. C.; Sun, M. H.; van Veldhoven, P. J.; Geluk, E. J.; Karouta, F.; Oei, Y. S.; Notzel, R.; Ning, C. Z.; Smit, M. K. *Opt. Express* **2009**, *17*, 11107–11112.
(26) Biagioni, P.; Huang, J. S.; Duo, L.; Finazzi, M.; Hecht, B. *Phys. Rev. Lett.* **2009**, *102*, 256801.
(27) Fromm, D. P.; Sundaramurthy, A.; Schuck, P. J.; Kino, G.; Moerner, W. E. *Nano Lett.* **2004**, *4*, 957–961.
(28) Sundaramurthy, A.; Schuck, P. J.; Conley, N. R.; Fromm, D. P.; Kino, G. S.; Moerner, W. E. *Nano Lett.* **2006**, *6*, 355–360.
(29) Prodan, E.; Radloff, C.; Halas, N. J.; Nordlander, P. *Science* **2003**, *302*, 419–422.
(30) Hao, F.; Nordlander, P.; Sonnefraud, Y.; Van Dorpe, P.; Maier, S. A. *ACS Nano* **2009**, *3*, 643–652.
(31) Verellen, N.; Sonnefraud, Y.; Sobhani, H.; Hao, F.; Moshchalkov, V. V.; Dorpe, P. V.; Nordlander, P.; Maier, S. A. *Nano Lett.* **2009**, *9*, 1663–1667.
(32) Christ, A.; Ekinci, Y.; Solak, H. H.; Gippius, N. A.; Tikhodeev, S. G.; Martin, O. J. F. *Phys. Rev. B* **2007**, *76*, 201405.
(33) Bachelier, G.; Russier-Antoine, I.; Benichou, E.; Jonin, C.; Del Fatti, N.; Vallee, F.; Brevet, P. F. *Phys. Rev. Lett.* **2008**, *101*, 197401.
(34) Liu, N.; Kaiser, S.; Giessen, H. *Adv. Mater.* **2008**, *20*, 4521–4525.
(35) Fedotov, V. A.; Rose, M.; Prosvirnin, S. L.; Papasimakis, N.; Zheludev, N. I. *Phys. Rev. Lett.* **2007**, *99*, 147401.
(36) Tang, L.; Miller, D. A. B.; Okyay, A. K.; Matteo, J. A.; Yuen, Y.; Saraswat, K. C.; Hesselink, L. *Opt. Lett.* **2006**, *31*, 1519–1521.

NL902850F